CrossMark

Dependence of O_2 and Ar_2 flow rates on the physical properties of ATO thin films deposited by atmospheric pressure chemical vapor deposition (APCVD)

M. R. Fadavieslam[1] (ORCID) · **S. Sadra[1]**

Abstract Antimony-doped tin oxide SnO_2:Sb thin films were fabricated through atmospheric pressure chemical vapor deposition at $T = 350$ °C on soda lime glass substrates. After preparing the thin films, the effects of oxygen and argon flow rates on the structural, optical, and electrical properties were investigated. The films were characterized by X-ray diffraction (XRD), scanning electron microscopy, atomic force microscopy, optical absorption (UV-Vis), and electrical resistance measurements using the two-point probe technique and the Hall effect. The results showed that the films contained uniform polycrystalline structures. Accordingly, the structural, morphological, optical, and electrical properties of the samples indicated the following effects: (a) Increasing the oxygen flow rate from 60 to 160 cc/min decreased the intensity of XRD peaks, the average roughness from 48.5 to 47.9 nm, the average transmission from 44 to 40 (in the visible region), the optical band gap from 3.74 to 3.66 eV, and the carrier mobility from 239.52 to 21.08 cm^2/V.S; moreover, it increased the average grain size from 74 to 79 nm, the thickness from 320 to 560 nm, the specific resistance from 3.38×10^{-2} to 14.9×10^{-2} Ω cm, the carrier concentration from 7.72×10^{17} to 1.99×10^{18} cm^{-3}, and the Seebeck coefficient from 47.2 to 57.85 μVk^{-1} (at 400 K). (b) Increasing the argon flow rate of 40 cc/min to 120 cc/min decreased the intensity of XRD peaks, the average size of grains from 88 nm to 61 nm, the optical band gap from 3.66 to 2.73 eV, the carrier concentration from 1.99×10^{18} to 1.73×10^{17} cm^{-3}, and the Seebeck coefficient from 57.85 to 36.59 μVk^{-1} (at 400 k); moreover, this increased the average roughness from 47.9 to 50.8 nm, the average transmission from 40 to 64 (in the visible region), thickness from 560 to 620 nm, specific resistance from 14.9×10^{-2} to 39.87×10^{-2} Ω cm, and carrier mobility from 21.08 to 90.61 μv/vs. (c) All thin films had degenerate n-type conductivity.

1 Introduction

Optoelectronic and photovoltaic devices and other energy applications require transparent conducting oxide (TCO) coatings with high transmission, high uniformity, low sheet resistance, and high substrate area. In recent years, transparent conductors have found major applications in many fields, such as active and passive electronics and optoelectronic devices, ranging from aircraft window heaters to charge-coupled imaging devices [1]. Tin oxide (SnO_2) films belong to a class of wide band gap semiconductors and are optically transparent in the visible part of the electromagnetic spectrum [2]. Generally, optically transparent materials are insulators, but the resistivity of SnO_2 varies from 10^{-4} to 10^6 Ω-cm, similar to most semiconductors [2]. Moreover, combining these two features results in potential TCOs. The combination is suitable for numerous applications, such as solar cell electrodes, light-emitting diodes, flat panel displays, antistatic coatings, touchscreens, organic light-emitting diodes, transparent electronics, resistors, gas sensors, solar cell coatings, transparent heating elements, and antistatic coatings [1–3]. The numerous applications of TCO in the different fields of science and technology make it an interesting material for research. The most commonly used TCO is tin-doped indium oxide (ITO) because of its good optical and electrical properties [3]. However, a drawback for using ITO is its high cost due to the scarcity of indium [4].

✉ M. R. Fadavieslam
   m.r.fadavieslam@du.ac.ir

[1] School of Physics, Damghan University, Damghan, Iran

Therefore, many attempts have been made to substitute these well-recognized materials. Today, SnO_2-doped materials are attracting attention because they are potential indium tin oxide (ITO) substitutes. Doping SnO_2 further widens its technological applications [5]. Hence, the interest is growing in modifying the structural, optical, and electrical properties of SnO_2 with a suitable dopant. Many dopants, such as W [6], Al [7], In [8], F [9], La [10], Ni [11], Pt [11], V [12], Pd [13], Fe [14], and Sb [15, 16], have been used to improve electrical properties of SnO_2 thin films. The Sb-doped tin oxide (ATO) thin film has been considered an ITO alternative due to its excellent heat resistivity [17]. Thus far, synthetic methods, such as electron beam, pulsed laser, sputtering, and carried out under vacuum conditions, have been developed to fabricate ATO thin films. However, research trends have changed from vacuum-based deposition methods to solution-based deposition approaches, such as photochemical techniques, sol–gel, chemical vapor deposition, spin coating, dip coating, and spray pyrolysis, because of their simplicity, scalability, and low-cost device manufacturing [16].

In this paper, we report the preparation and characterization of antimony-doped SnO_2 thin films. We used the atmospheric pressure chemical vapor deposition (APCVD) method to deposit the thin films. Moreover, we studied the effects of oxygen and argon flow rates on the structural, optical, and electrical characteristics of ATO thin films.

2 Experimental

2.1 Sample preparation

ATO thin films were studied in this work. The films were prepared using precursors, such as $SnCl_2 \cdot 5H_2O$ and $SbCl_3$. We used two different gases to carry the primary materials, with each being controlled by a separate flow meter. Oxygen was used as the carrier gas of H_2O and argon as the carrier gas of $SnCl_2 \cdot 5H_2O$ and $SbCl_3$. A horizontal ceramic holder measuring 2.5×7.5 cm was used to obtain our glass substrate. Films would not grow at substrate temperatures lower than 340 °C, and uniform films are obtained at 350 °C. We fixed the temperatures for vaporizing water, vaporizing tin chloride and antimony chloride, and substrate temperatures at 60, 250, and 350 °C, respectively. To study the effects of oxygen and argon flow rates, we did the experiments five times with five different deposition conditions, as shown in Table 1.

2.2 Structural and optical characterization of films

The structural properties of the films were determined by X-ray diffraction (XRD) using a D8 Advance Bruker system ($\lambda = 0.15405$ nm and 2θ is in the range 10°–70°). The

Table 1 Naming convention here issued to make comparing easier in this manuscript

Number	Sample name	Oxygen flow rate (cc/min)	Argon flow rate (cc/min)
1	O60Ar40	60	40
2	O120Ar40	120	40
3	O160Ar40	160	40
4	O160Ar80	160	80
5	O160Ar120	160	120

average crystalline grain size was calculated using Scherrer's formula based on the XRD patterns [16]:

$$D = \frac{k\lambda}{\delta_{\mathrm{w}} \cos\theta} \tag{1}$$

where D is the average crystalline (grain) size, K is a constant (~ 1), λ is the X-ray wavelength, δ_{w} is the full-width at half-maximum (FWHM) of XRD peaks, and θ is the Bragg angle. The surface morphology of the films was investigated using a scanning electron microscopy (SEM, KYKY EM 3200) and an atomic force microscopy (AFM; 95-50-E DME).

For measuring the optical absorption and transparency of the films, we used a Unico 4802 UV-Vis double beam spectrophotometer at a wavelength range of 300–1100 nm at room temperature.

The direct optical band gap was obtained by UV-Vis measurements, plotting $(\alpha h v)^2$ versus photon energy ($h v$) and using Tauc's equation [18]:

$$(\alpha h v)^2 = \beta(h v - E_{\mathrm{g}}) \tag{2}$$

where α is the absorption coefficient, β is a constant, and E_{g} is the direct band gap of the material.

2.3 Electrical measurements

To measure electrical properties of the films, the two ends of the samples were coated with aluminum using thermal evaporation in a vacuum. The electrical resistivity of the films on the non-conducting side of the glass was assessed using the DC two-probe method.

By applying a temperature gradient between the two ends of the samples at 300–500 K, the thermoelectric emf values of the thin films were measured [19]. To heat one side (hot side), an electrical heater with an electrical power of 300 W was used; moreover, an ice water bath was used for cooling the other side (cold side). The open circuit thermovoltage produced from the sample was measured using a digital micro-voltmeter. Due to the temperature difference between the two ends of the samples, the carriers were transported from the hot to the cold end. This step created an electric field that gave rise to the
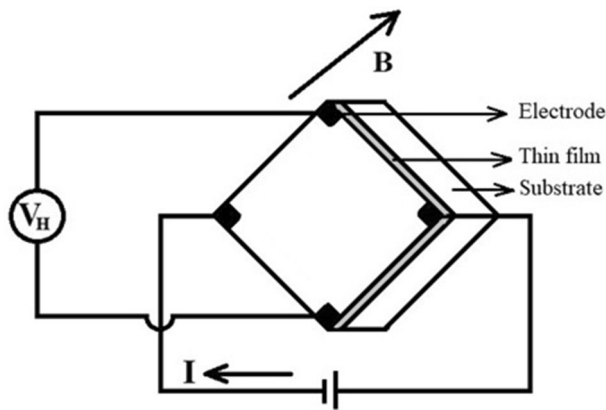
Fig. 1 Basic setup for the van der Pauw configuration

thermovoltage across the ends. The produced thermovoltage was directly proportional to the applied temperature gradient to the two ends of the semiconductor thin films. The signs of the charge carriers were obtained from the signs of the potentiometer terminals connected to the two ends of the samples. Negative and positive terminals were connected to the hot and cold ends for this measurement, respectively. Thus, the films showed n- or p-type conductivity. According to the Seebeck effect, thermoelectric power (TEP) is calculated by [18]:

$$\varepsilon = \alpha \Delta T \tag{3}$$

where ε is the emf, α is the Seebeck coefficient, and ΔT is the temperature difference between the sample edges. The thermoelectromotive force ($\Delta V = \varepsilon$) was proportional to the temperature difference between the sample edges (ΔT). Seebeck coefficients (α) were derived by calculating the slope of the thermoelectric emf versus the temperature difference between the hot and the cold sample ends.

Finally, using the Hall effect method, the type and majority carrier density of the samples were measured. Hall effect data were measured by employing the van der Pauw configuration. A schematic view of the apparatus is shown in Fig. 1.

2.4 Structural characterization

Figures 2 and 3 show the XRD patterns of the samples in three different oxygen flux rates and three different argon flux rates, respectively. All samples had tetragonal polycrystalline structures with three phases, namely SnO_2, Sn_3O_4, and Sb_2O_3. Other forms, namely, the compound phases of either Sn or Sb, were not seen in the pattern, which means that the chemical reaction was completed.

As shown in Fig. 2, by decreasing the oxygen flux rate from 160 to 60 cc/min, in general, the intensity of the peaks in the $(0\bar{2}1)$ plate, which is the preferred orientation,
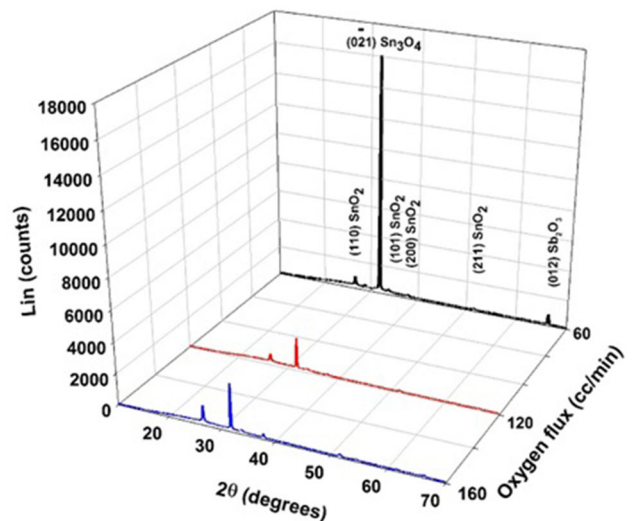

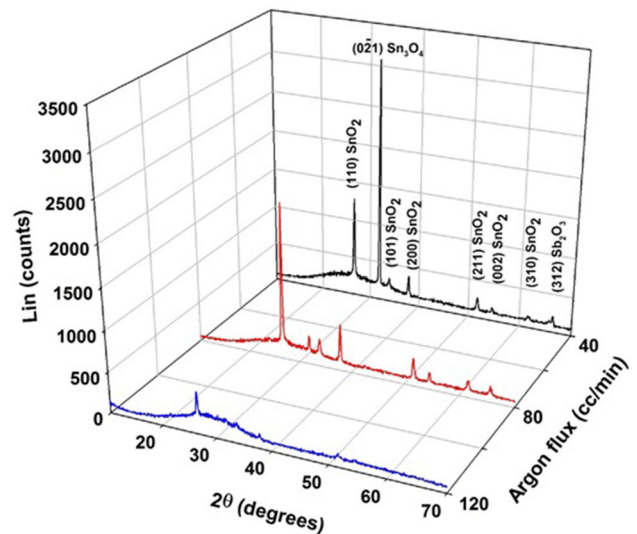Fig. 2 X-ray diffraction patterns of thin films prepared by various oxygen flow rate

Fig. 3 X-ray diffraction patterns of thin films prepared by various argon flow rate

increased significantly. The maximum peak is related to Sn_3O_4 in the $(0\bar{2}1)$ plate in the 60 cc/min oxygen flux. As observed in Fig. 3, by decreasing the argon flux rate from 120 to 40 cc/min, in general, the intensity of the peaks in the $(0\bar{2}1)$ plate, which is the preferred orientation, increased significantly. The maximum peak is related to Sn_3O_4 in the $(0\bar{2}1)$ plate in the 40 cc/min argon flux. As shown in Figs. 2 and 3, the maximum peaks in all curves were related to O60Ar40 and O160Ar40, which had 320 and 560 nm thicknesses, respectively. The XRD peak intensities can be related to the crystallinity and film thickness. A thick film (of the same level of crystallinity)

Table 2 XRD results for thin films

Sample name	2θ(°)	hkl	Phase	Lattice distance (Å)	Mean grain size (nm)
Effect of oxygen flux					
O60Ar40	26.597	110	SnO_2	3.34881	30.12
	31.856	$(0\bar{2}1)$	Sn_3O_4	2.80694	33.72
O120Ar40	26.662	110	SnO_2	3.34078	25.92
	31.874	$(0\bar{2}1)$	Sn_3O_4	2.80535	34.71
O160Ar40	26.64	110	SnO_2	3.34347	29.9
	31.866	$(0\bar{2}1)$	Sn_3O_4	2.80603	33.72
Effect of argon flux					
O160Ar40	26.64	110	SnO_2	3.34347	29.9
	31.866	$(0\bar{2}1)$	Sn_3O_4	2.80603	33.72
O160Ar80	26.616	110	SnO_2	3.34642	29.68
	31.854	$(0\bar{2}1)$	Sn_3O_4	2.80705	27.81
O160Ar120	26.651	110	SnO_2	3.34212	25.92
	31.96	$(0\bar{2}1)$	Sn_3O_4	2.79802	19.31
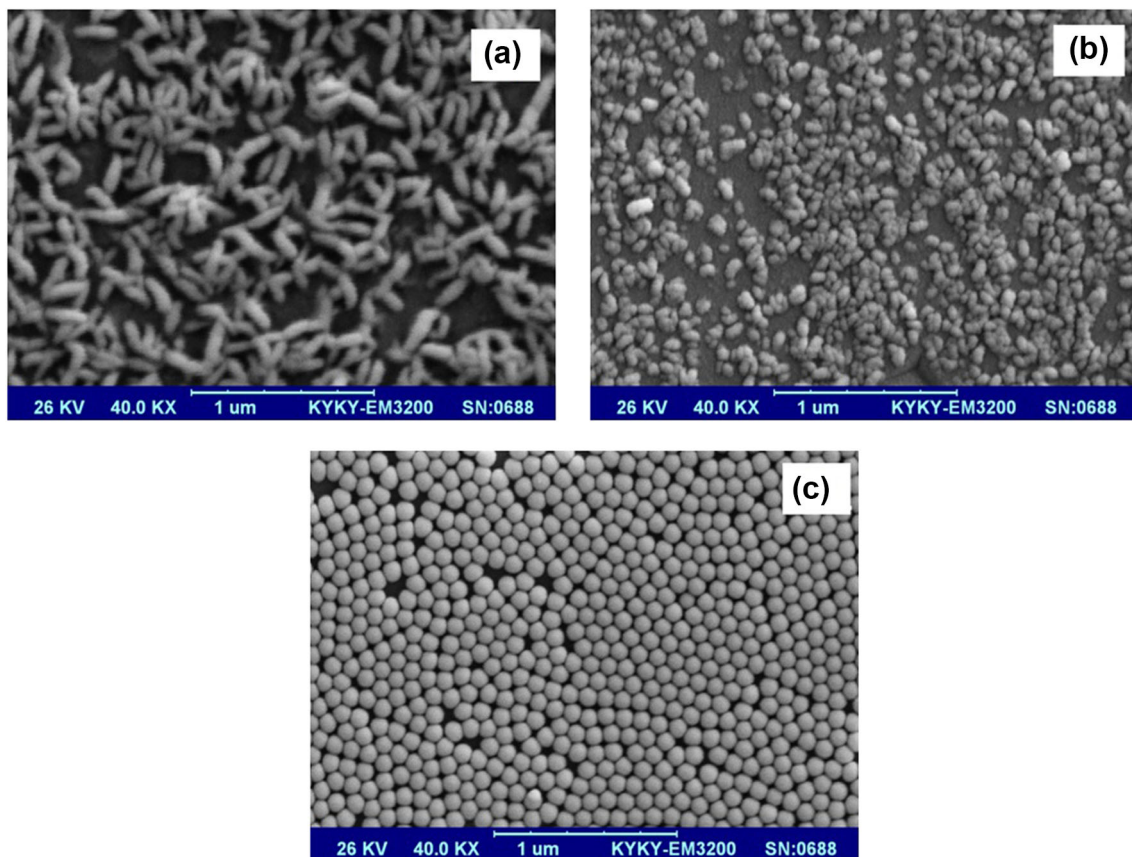
Fig. 4 SEM image of thin films prepared by **a** 60 cc/min, **b** 120 cc/min, and **c** 160 cc/min oxygen flow rate

will give a high-intensity signal. To determine the variation of the mean crystallite size (D) with the oxygen and argon flux values, we calculated the crystallite sizes oriented along the (110) and (0$\bar{2}$1) planes using Scherrer's formula,

as shown in Table 2. The results showed that the average crystallite size was 30 nm. Comparing the XRD results of the oxygen and argon flux, we concluded that, first, the grain size and maximum intensity of the oxygen flux would
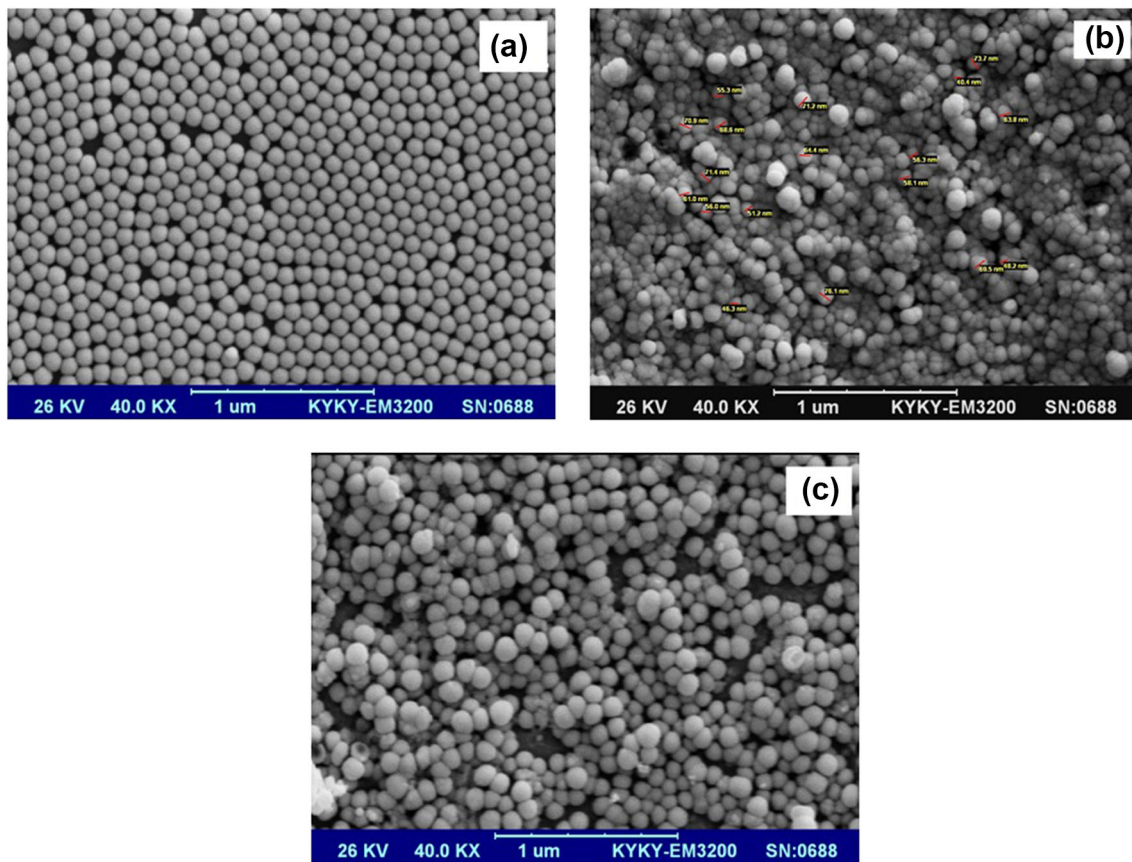
Fig. 5 SEM image of thin films prepared by **a** 40 cc/min, **b** 80 cc/min, and **c** 120 cc/min argon flow rate

be higher than the results of the argon flux. Second, when the argon flux rate decreased from 120 to 40 cc/min, the chemical reactions increased. This effect was due to the peak intensity.

2.5 Surface morphology

Figure 4 shows the SEM illustrations of the three samples with different oxygen fluxes. Based on these observations, the sample O60Ar40 has maggot-like shapes, and the increased oxygen fluxes changed the maggot-like shapes to granular. The average grain sizes in the 60, 120, and 160 cc/min oxygen fluxes were 74, 48, and 79 nm, respectively. Figure 5 presents the SEM illustrations of the three samples with different argon fluxes. These images show that the samples have granular shapes, and decreasing the argon fluxes improved the granular shape of grains. The average grain sizes in the 40, 80, and 120 cc/min argon fluxes were 88, 79, and 61 nm, respectively. The increased argon flow rate decreased the average grain size; moreover, the increase in oxygen flow rate initially decreased and

then increased the average grain size. This change was noted with the results of XRD diffraction samples for page (110) matched.

Figures 6 and 7 show the AFM images of the thin films with different oxygen and argon fluxes, respectively. The average roughness values for O60Ar40, O120Ar40, and O160Ar40 samples were 48.5, 45.3, and 47.9 nm, respectively. The average roughness values for O160Ar40, O160Ar80, and O160Ar120 samples were 47.9, 73.8, and 50.8 nm, respectively. Based on these observations, sample O120Ar40 showed homogeneity and a higher order compared with the other layers, and its average roughness was lower compared with the other layers.

2.6 Optical characterization

Optical transmittance of the samples was investigated in the wavelength range of 300–1100 nm. Figures 8 and 9 present the results for the oxygen and argon flow rates, respectively. For the 60, 120, and 160 cc/min oxygen fluxes, the average transmission values in the visible region
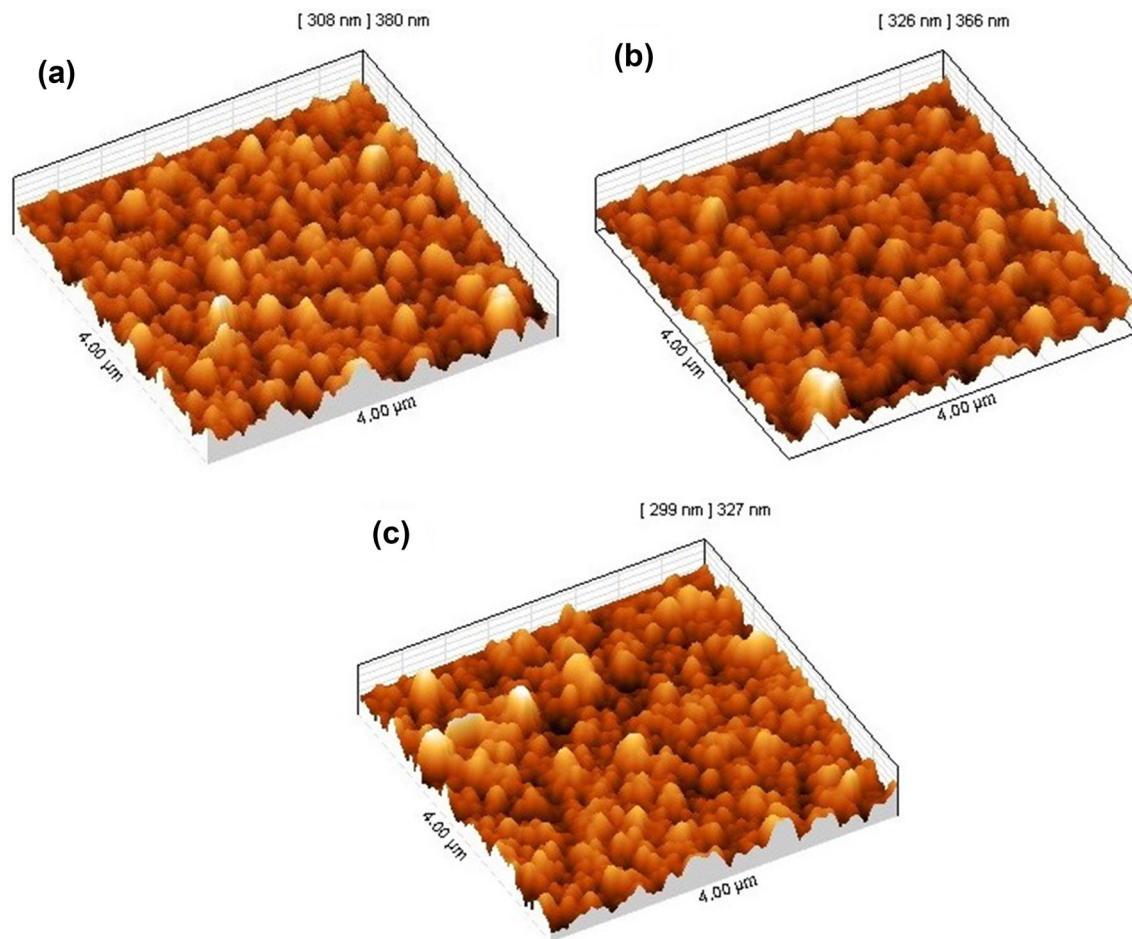
Fig. 6 AFM image of thin films prepared by **a** 60 cc/min, **b** 120 cc/min, and **c** 160 cc/min oxygen flow rate

were 44, 58, and 40%, respectively. Moreover, the 40, 80, and 120 cc/min argon fluxes indicated 40, 17, and 64%, respectively.

The maximum transmittance of the thin films was approximately 64%, which was the value for the film deposited with oxygen and argon flow rates at 160 and 120 cc/min. High transparency is associated with good structural homogeneity. In transparent metaloxides, the metal-to-oxygen ratio and crystal orientation determine the percentage of transmittance. The low transmittance of thin films was due to the (1) increased photon scattering by the crystal defects or that their layered structures reduced the free charge mobility [20]; (2) reflection losses that included specular and scattered (diffuse) components and due to surface roughness; and (3) homogeneities in the film in terms of unreacted chemical species generated during the complex CVD process [21].

The optical band gap of the films in various oxygen and argon fluxes was determined from the plot of $(\alpha h\vartheta)^2$ versus $h\vartheta$, as shown in Figs. 10 and 11, respectively. The plots were linear and indicated a direct optical transition. The average direct band gap of the thin films, as shown in the figures, was 3.7 eV, which was close to the value of 3.80 eV observed in bulk SnO_2 [6]. The results of the optical characterization of the thin films are shown in Table 3.

2.7 Electrical characterization

Table 4 summarizes the results of the electrical measurements of thin films. Hall effect measurements defined the majority of carriers to be n-type. The room temperature variations of resistivity (ρ), carrier density (n), and Hall mobility (μ) against the oxygen and argon flow rates are shown in Figs. 12 and 13, respectively. Increasing the oxygen or argon flow rate increased the resistivity. These results can be explained by XRD patterns. By increasing the oxygen or argon flux rate, (1) the peak intensities increase significantly and cause crystallites to decrease, and (2) the decrease in crystallite and grain sizes, which will increase the grain boundary, increase resistivity [22]. When
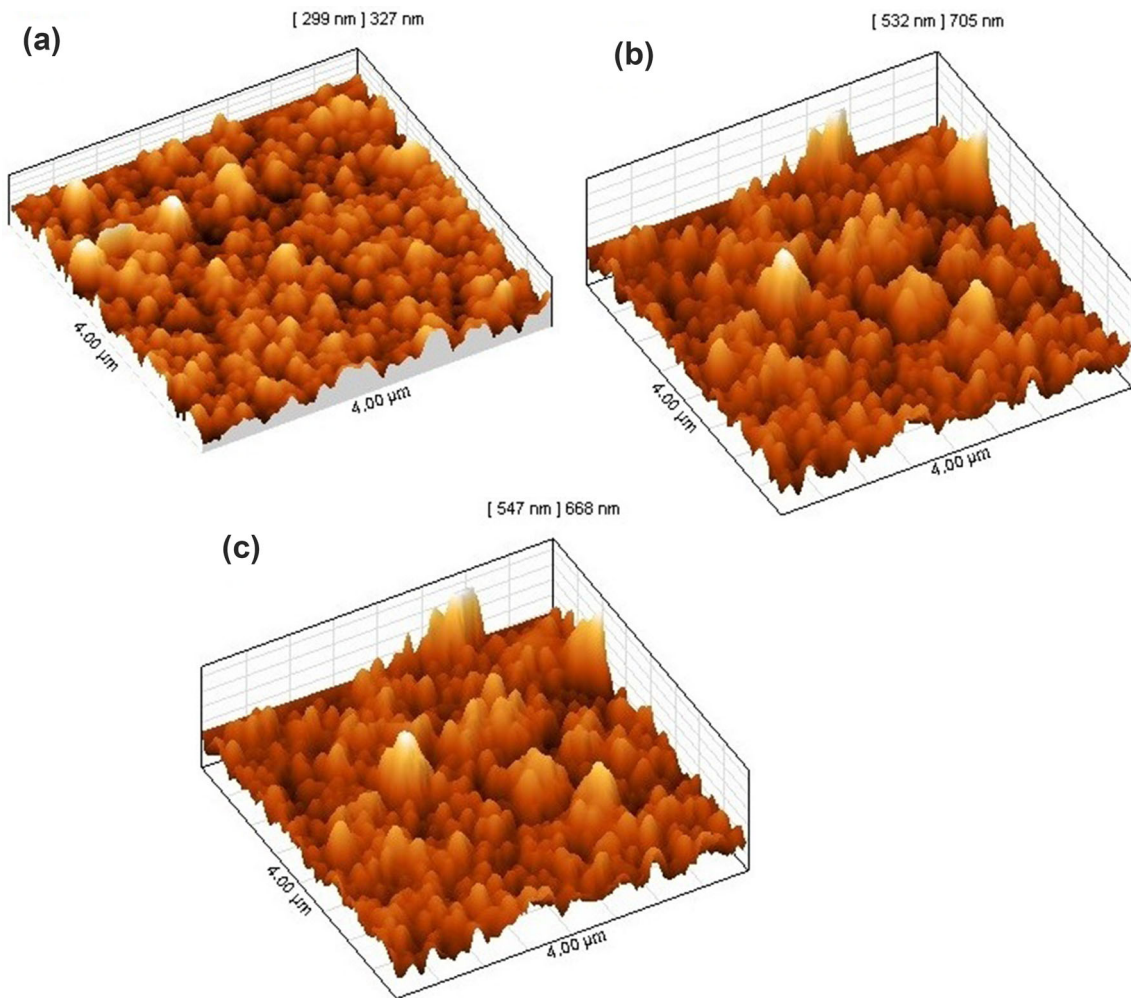
(a) [299 nm] 327 nm

(b) [532 nm] 705 nm

(c) [547 nm] 668 nm

Fig. 7 AFM image of thin films prepared by **a** 40 cc/min, **b** 80 cc/min, and **c** 120 cc/min argon flow rate
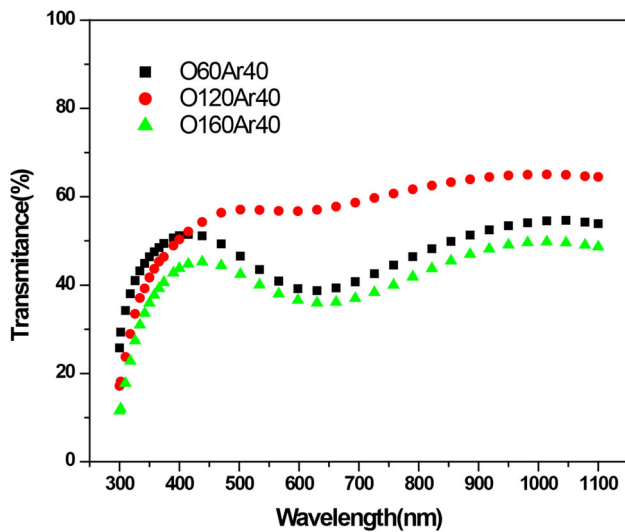

Fig. 8 Variation of transmittance versus the wavelength of thin films prepared by various oxygen flow rate
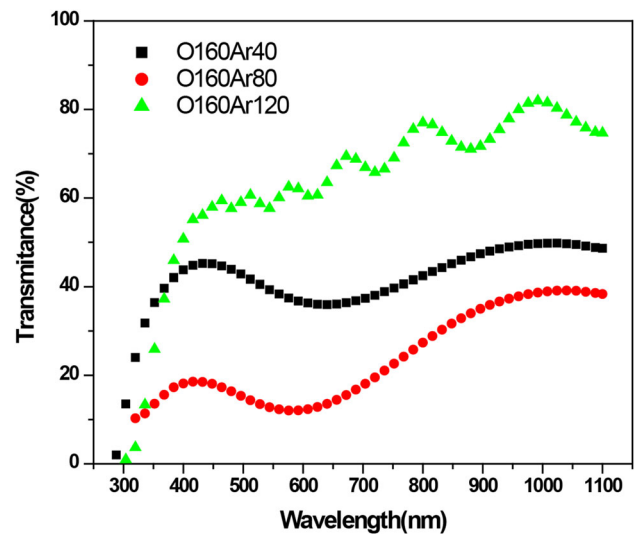
Fig. 9 Variation of transmittance versus the wavelength of thin films prepared by various argon flow rate
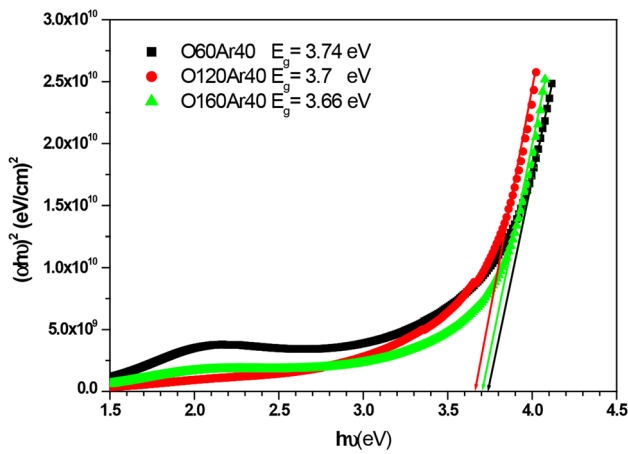
Fig. 10 Plots of $(\alpha h\vartheta)^2$ versus $h\vartheta$ of thin films prepared by various oxygen flow rate
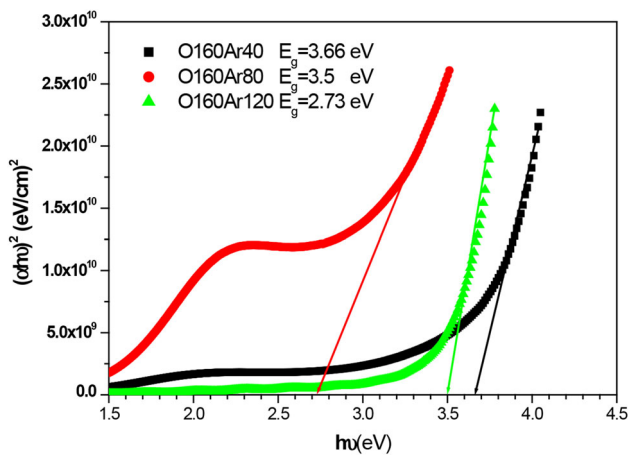

Fig. 11 Plots of $(\alpha h\vartheta)^2$ versus $h\vartheta$ of thin films prepared by various argon flow rate

Table 3 Results of optical measurements of thin films

Sample name	Thickness (nm)	Average transmittance in the visible spectra	Optical gap (eV)
Effect of oxygen flux			
O60Ar40	320	44	3.74
O120Ar40	370	58	3.7
O160Ar40	560	40	3.66
Effect of argon flux			
O160Ar40	560	40	3.66
O160Ar80	430	17	3.5
O160Ar120	620	64	2.73

Sb atoms were substituted into the Sn^{4+} sites of the SnO_2 lattice in two different oxidation states, namely Sb^{5+} and Sb^{3+}, in the Sb^{5+} state, they acted as donors by creating excess electrons. Consequently, the film resistivity decreases. Moreover, further Sb addition introduced Sb^{3+}

Table 4 Results of electrical measurements of thin films

| Sample name	Sheet resistance (kΩ/□)	Resistivity (Ω cm) $\times 10^{-2}$	Carrier concentration (cm^{-3})	Carrier mobility (cm^2/VS)	Seebeck coefficient (μVK^{-1}) $T = 400$ K
Effect of oxygen flow rate					
O60Ar40	1.06	3.38	7.72×10^{17}	239.52	47.2
O120Ar40	1.95	7.22	1.39×10^{18}	62.27	42.64
O160Ar40	2.66	14.9	1.99×10^{18}	21.08	57.85
Effect of argon flow rate					
O160Ar40	2.66	14.9	1.99×10^{18}	21.08	57.85
O160Ar80	6.29	27.05	5.07×10^{17}	45.57	48.14
O160Ar120	6.43	39.87	1.73×10^{17}	90.61	36.59
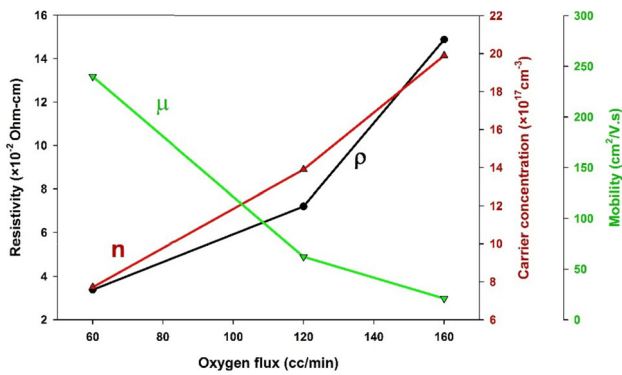
Fig. 12 Variations of resistivity (ρ), carrier density (n), and Hall mobility (μ) as a function of oxygen flow rate in the thin films
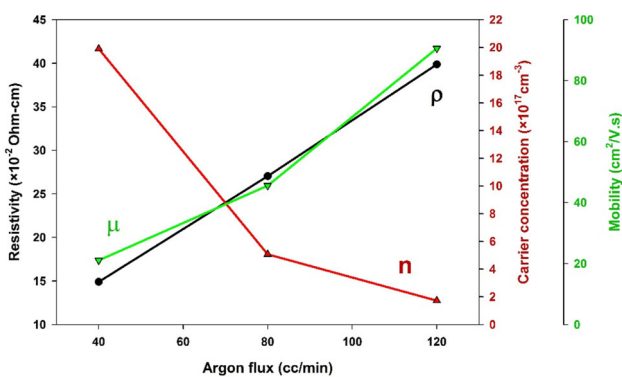

Fig. 13 Variations of resistivity (ρ), carrier density (n), and Hall mobility (μ) as a function of argon flow ratein the thin films

Fig. 14 Variation of thermoelectric emf versus temperature difference of thin films prepared by various oxygen flow rate

Fig. 15 Variation of thermoelectric emf versus temperature difference of thin films prepared by various argon flow rate

sites that acted as acceptors and compensated the donors created by the Sb^{5+} species, thereby increasing resistivity [22]. Increasing the oxygen or decreasing the argon flow rate carrier reduces the mobility. The increase in carrier mobility can be due to the grain growth. The increase in grain size reduces the number grain barrier traps, thereby resulting in low dispersion in the grain barriers, which then increases carrier mobility.

The variation of the thermoelectric emf versus the temperature difference for thin films in various oxygen and argon fluxes is shown in Figs. 14 and 15, respectively. Moreover, the Seebeck coefficients at $T = 400$ K are reported in Table 2. Thermo-electrical effect measurements indicated n-type conductivity for the thin films. The thermoelectric emf depended on the location of the material's Fermi energy, type of scattering mechanism, and charge carriers encountered. The effect increased as the Fermi energy moved further into the energy gap from the bottom edge of the conduction band. These values concluded that the reduced carrier concentration increased the
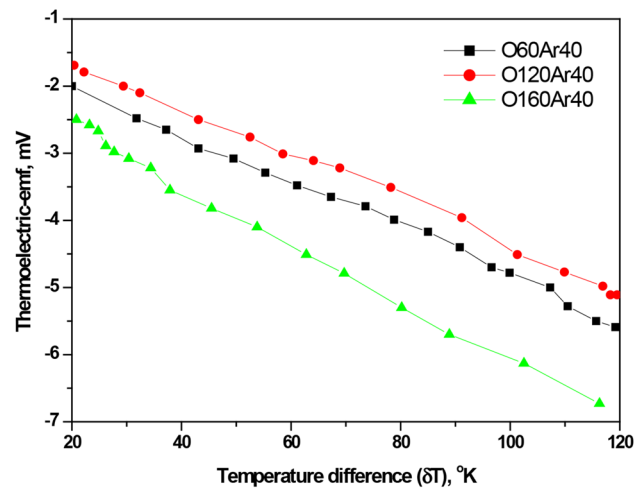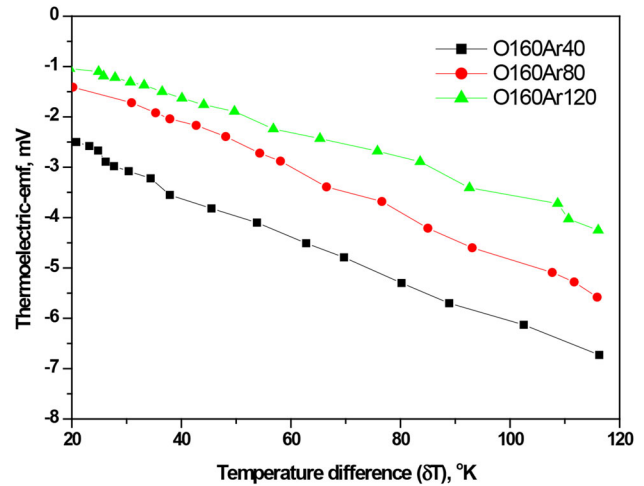
Seebeck coefficient. Thus, the high crystalline and crystallite sizes increased the thermoelectric emf of thin films.

3 Conclusion

In this paper, we reported the preparation and characterization of SnO$_2$:Sb thin films. Thin films were deposited onto a glass substrate under a fixed substrate temperature of 350 °C at different oxygen and argon flow rates using a simple and inexpensive method of atmospheric pressure chemical vapor deposition. The maximum transmittance of the thin films obtained at approximately 64% resulted from the film deposited in the oxygen and argon flow rates of 160 and 120 cc/min,

respectively. The average optical band gap of the films was 3.47 eV. The results of the Hall effect and thermo-electric emf showed that majority of the carriers were n-type, and the carrier concentration varied from 1.73×10^{17} to 1.99×10^{18} cm^{-3}. Moreover, increasing the oxygen flow rate increased the mean grain size, specific resistance, and Seebeck coefficient (at 400 K), as well as reduced the XRD peaks, optical band gap, and surface roughness. Furthermore, increasing the argon flow rate increased the surface roughness and specific resistance, as well as decreased the mean grain size, optical band gap, and Seebeck coefficient (at 400 K).

References

1. D. Zhang, Z. Deng, J. Zhang, L. Chen, Mater. Chem. Phys. **98**, 353–357 (2006)
2. M.P.S. Rana, F. Singh, S. Negi, S.K. Gautam, R.G. Singh, R.C. Ramola, Ceram. Int. **42**, 5932–5941 (2016)
3. J. Montero, C. Guillén, J. Herrero, Surf. Coat. Technol. **211**, 37–40 (2012)
4. J. Boltz, D. Koehl, M. Wuttig, Surf. Coat. Technol. **205**, 2455–2460 (2010)
5. S. Yu, W. Zhang, L. Li, D. Xu, H. Dong, Y. Jin, Appl. Surf. Sci. **286**, 417–420 (2013)
6. Y. Huang, Q. Zhang, G. Li, M. Yang, Mater. Charact. **60**, 415–419 (2009)
7. J.S. Bhat, K.I. Maddani, A.M. Karguppikar, S. Ganesh, Nucl. Instrum. Methods Phys. Res. Sect. B Beam Interact. Mater. Atoms **258**, 369–374 (2007)
8. Z.B. Zhou, R.Q. Cui, Q.J. Pang, Y.D. Wang, F.Y. Meng, T.T. Sun, Z.M. Ding, X.B. Yu, Appl. Surf. Sci. **172**, 245–252 (2001)
9. A.V. Moholkar, S.M. Pawar, K.Y. Rajpure, C.H. Bhosale, J.H. Kim, Appl. Surf. Sci. **255**, 9358–9364 (2009)
10. A. Marsal, A. Cornet, J.R. Morante, Sens. Actuators B Chem. **94**, 324–329 (2003)
11. M. Gaidi, B. Chenevier, M. Labeau, J.L. Hazemann, Sens. Actuators B Chem. **120**, 313–315 (2006)
12. C.-T. Wang, M.-T. Chen, Mater. Lett. **63**, 389–390 (2009)
13. Y. Feng, R. Yao, L. Zhang, Mater. Chem. Phys. **89**, 312–315 (2005)
14. S. Chakraborty, A. Sen, H.S. Maiti, Sens. Actuators B Chem. **115**, 610–613 (2006)
15. D. Zhang, L. Tao, Z. Deng, J. Zhang, L. Chen, Mater. Chem. Phys. **100**, 275–280 (2006)
16. M.R. Fadavieslam, J. Mater. Sci. Mater. Electron. **27**, 4943–4950 (2016)
17. S.Y. Lee, B.O. Park, Thin Solid Films **510**, 154–158 (2006)
18. M.R. Fadavieslam, H. Azimi-Juybari, M. Marashi, J. Mater. Sci. Mater. Electron. **27**, 921–930 (2016)
19. G.S. Nolas, J. Sharp, H.J. Goldsmid, *Thermoelectric Basic Principles and New Materials Development* (Springer, Berlin, 2001)
20. A.R. Babar, K.Y. Rajpure, J. Anal. Appl. Pyrolysis **112**, 214–220 (2015)
21. A.R. Babar, S.S. Shinde, A.V. Moholkar, C.H. Bhosale, J.H. Kim, K.Y. Rajpure, J. Alloys Compd. **505**, 416–422 (2010)
22. R. Outemzabet, N. Bouras, N. Kesri, Thin Solid Films **515**, 6518–6520 (2007)